Chapter 4 Rotor-axial Eulerian laser Doppler vibrometry applied to a five-blade axial-flow test rotor

4.1 Introduction

This chapter extends the work of Chapter 3 to a multi-blade test rotor to verify the ability of the proposed technique to identify damaged blades from among healthy blades. When considering a multi-blade rotor, it becomes necessary to take into account the effects of global blade vibration modes since damage on one blade affects the dynamics of the remaining blades and *vice versa*. As a result, trends may be identified from the undamaged blades which in turn may lead to the erroneous identification of damaged blades. A robust signal processing approach that accurately indicates blade damage is therefore required.

The first section of this chapter focuses on the experimental test setup and testing procedure. The procedure was done in two separate phases to consider damage on a single blade and damage on multiple blades consecutively. The effects on the blade-forcing frequency spectrum by blade-spacing variation due to manufacturing tolerances are studied and it is shown that these effects have to be taken into account during simulations using a FEM.

During experimental testing, high response levels were observed in both TLDV and ELDV measurements at certain damage cases and rotor speeds, similar to those reported in Section 3.3. To investigate this phenomenon, a FEM of the test rotor is constructed and subsequently the Root-Mean-Square (RMS) values of the measurements are shown to be promising blade health indicators.

Results from signal processing on the experimental ELDV measurements at various rotor speeds ranging from 720 RPM to 1440 RPM, are discussed in the next section. It is shown that statistical trend properties of MAUPATs as well as RMS and correlation coefficient trends are useful parameters in identifying damaged blades and monitoring degradation in these blades. In addition, multiple ELDV measurement positions are demonstrated to be advantageous to achieving robust results. After the training of ANNs with these parameters, it is proven that ELDV measurements can be used to accurately identify and quantify blade damage from amongst healthy blades.

Finally, it is verified experimentally that the first natural frequency of the individual blades can be accurately estimated from run-up and run-down ELDV measurements.

4.2 Test setup

The test rotor of Section 3.2 was again employed and installed with five straight, flat blades. The test rotor was driven directly by the speed-controlled motor at speeds of 720, 960, 1200 and 1440 RPM during testing. As previously, a piezoelectric dynamic pressure sensor measured the back-pressure at the nozzle arising from the airflow blockage caused by the blade during rotation. Due to manufacturing tolerances of the blade-clamp interfaces, it was necessary to use epoxy to eliminate gaps between the blade and clamp surfaces prior to clamping. This was found to minimize the variation in the natural frequencies of the blades, arising from differences in the clamping boundary conditions.

Prior to ELDV and TLDV testing, the natural frequencies of the individual rotor blades were obtained from stationary modal testing. Each blade was individually tested using a modal hammer as excitation and the Polytec PSV300 laser vibrometer for response measurements. This choice of excitation and measurement technique minimized any alteration in structural mass, thereby ensuring accurate FRFs. These FRFs were furthermore used for updating the rotor FEM.

As in Chapter 3, damage was simulated in various blades by increasing the depth of a slot cut in the blades' leading edges, close to the blade roots. Testing was conducted in two phases. During the first phase, damage was introduced on blade #1 only, whereas in the second phase, damage was considered on blade #3 and blade #5 simultaneously at different damage-increment rates. The damage cases considered are schematically depicted in Figure 46.

Due to manufacturing tolerances, variation was present in the spacing of the blades in both axial and circumferential directions. This affected the forcing frequency spectrum of the blades and in particular resulted in energy being introduced at higher rotor orders (Ewald et al., 1971). This spectrum can be estimated from the measured pressure pulses as demonstrated by the PSD in Figure 47 for 720 RPM, showing the first 16 harmonics. For this reason, it was important to ensure that the relative timings between pulse peaks used in the FEM correlated with those of the measured pressure pulses.
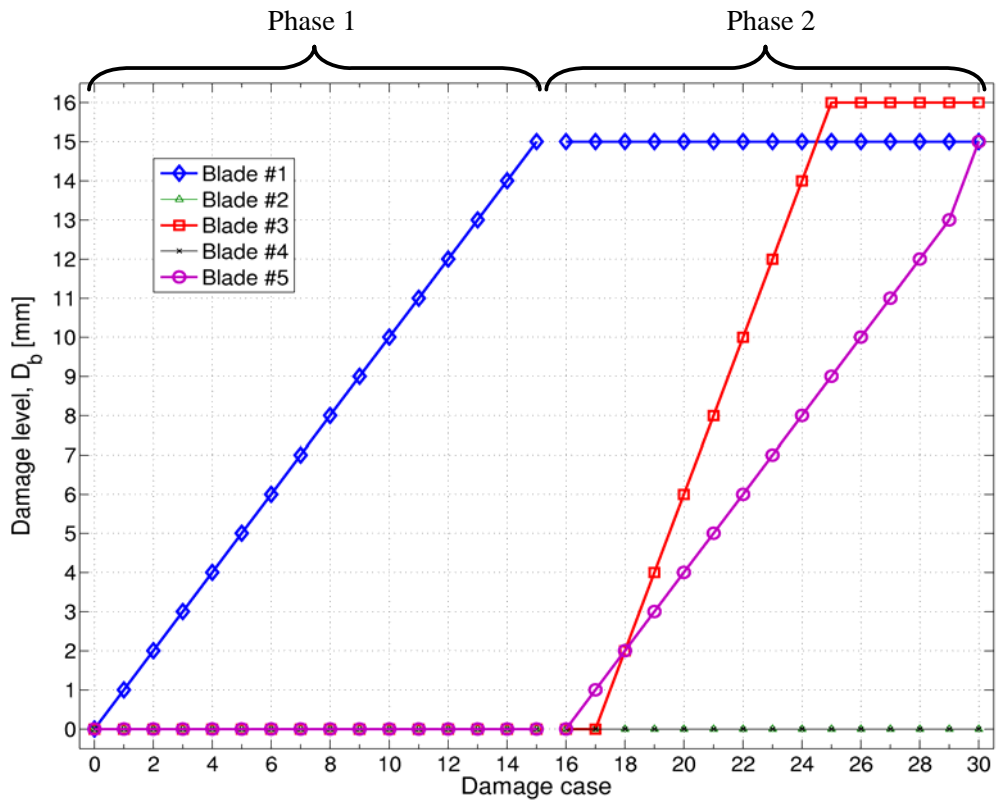
Phase 1   Phase 2

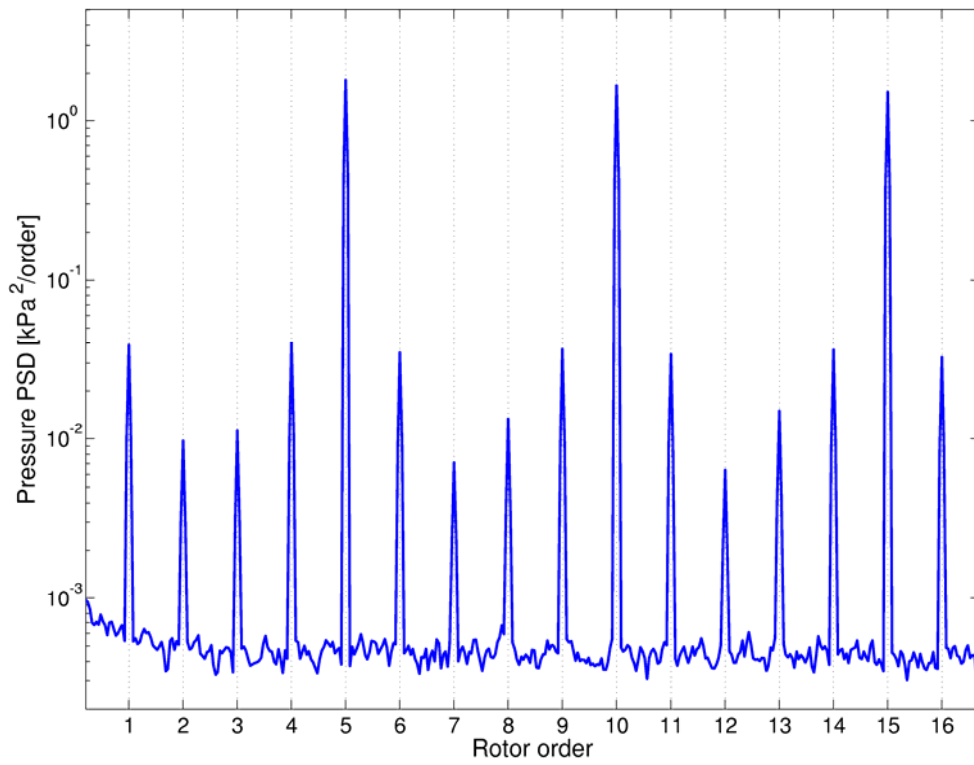Figure 46: Damage cases considered during testing

Figure 47: Pressure pulse harmonics

4.3 Test control and measurement

During ELDV and TLDV testing, data acquisition and vibrometer mirror control were again accomplished with LabView, using a National Instruments PCI-6110 card. The shaft encoder signal of 5000 PPR was used as a clock signal to perform position-based sampling, thus simplifying data post-processing. A schematic layout of the LabView algorithm used is given in Figure 48.
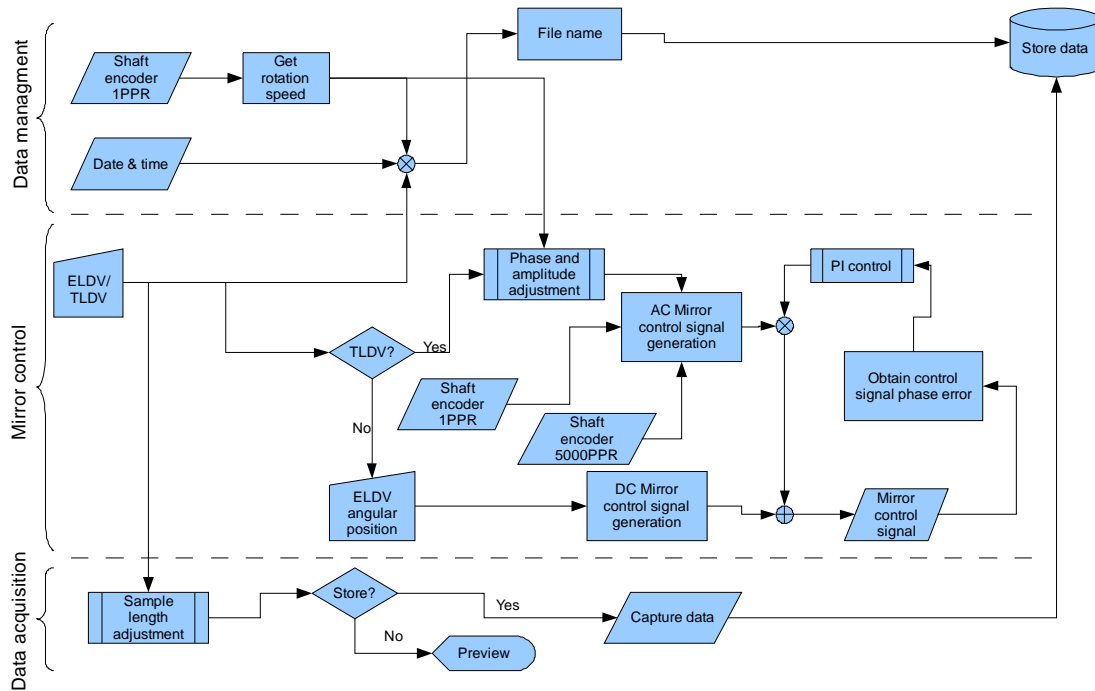

Figure 48: Schematic layout of LabView VI file for control and acquisition

TLDV measurements on the test rotor were available over nearly 180° as seen in Figure 49.   Since triggering is only available in edge-detection mode for this particular National Instruments card, any spurious peaks of amplitudes as low as 0.2 V in the shaft encoder signal caused erroneous clock pulse incrementation. It was therefore necessary to incorporate a Proportional-Integral (PI) control loop in the LabView algorithm used. Figure 50 compares the control signal phase error with and without implementation of the PI control loop at a rotation speed of 600 RPM. The initial 12.6^o phase angle errors that are visible from this figure result from the dynamic phase lag of the mirror-servo system.
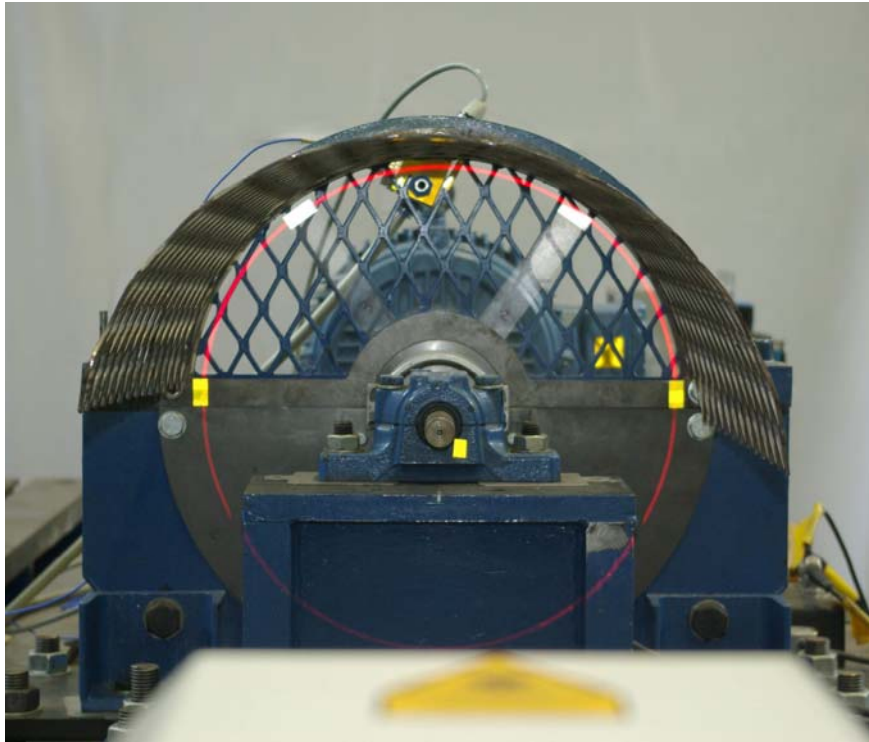
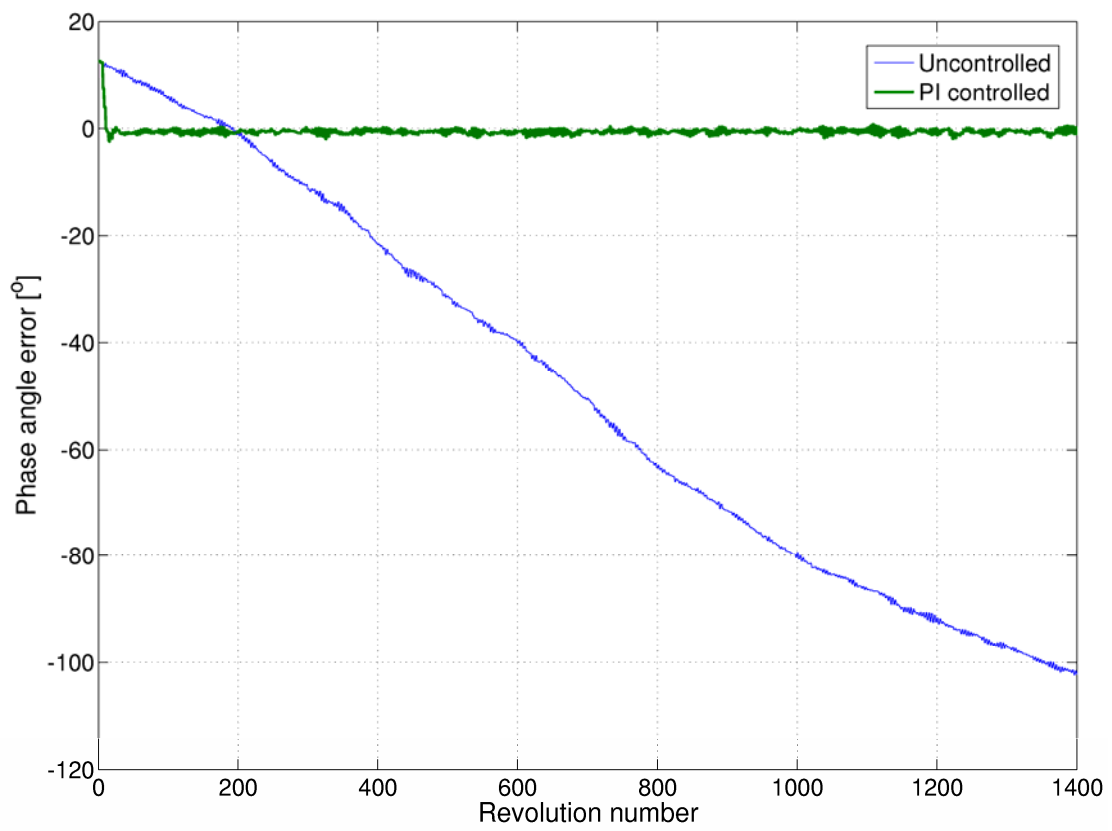**Figure 49: TLDV implementation**

Figure 50: TLDV PI control

Two measurement positions, namely A and B, were considered during ELDV testing (see Figure 51(a) and Figure 51(b) respectively). At position A, the ELDV forced-vibration signature is available as the blade passes in front of the nozzle (i.e. at position A, the air impinges on the blade for the duration of each individual ELDV measurement). Just after passing the nozzle, the free vibration ELDV signature is available at position B (i.e. no impingement by the air-jet.) The purpose of considering these two positions was firstly to determine the sensitivity of the proposed data analysis approach to measurement position. Secondly, it was used to investigate possible advantages of using multiple ELDV measurement positions for on-line condition monitoring.
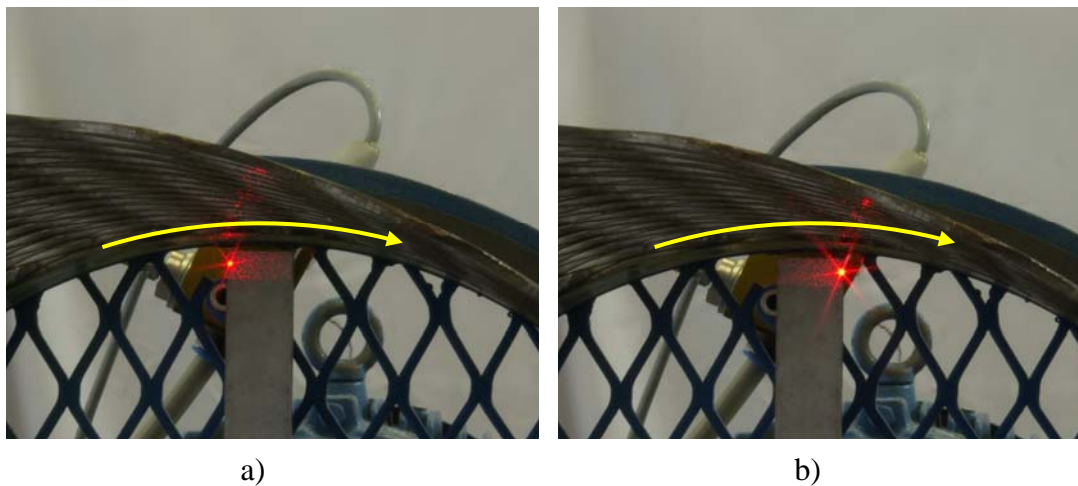
a)   b)

Figure 51: (a) ELDV position A; (b) ELDV position B

As in chapter 3, the SLDV was set to measure at a 125 mm/s/V sensitivity with the tracking filter option disabled. As mentioned earlier in section 4.3, position based sampling was performed using the shaft encoder 5000 PPR signal, resulting in the minimum sampling frequency used during testing being about 60 kHz. For this reason, the 20 kHz low-pass filter option was selected on the SLDV controller.

4.4 FEM

A FEM of the test rotor was constructed as shown in Figure 52. The blades were modelled with shell elements while the hub and shaft were modelled with solid and beam elements respectively. Beam-solid and shell-solid element coupling was accomplished with Multi-Point Constraint (MPC) elements. Damage was again simulated in the model by deleting appropriate elements in the blades.
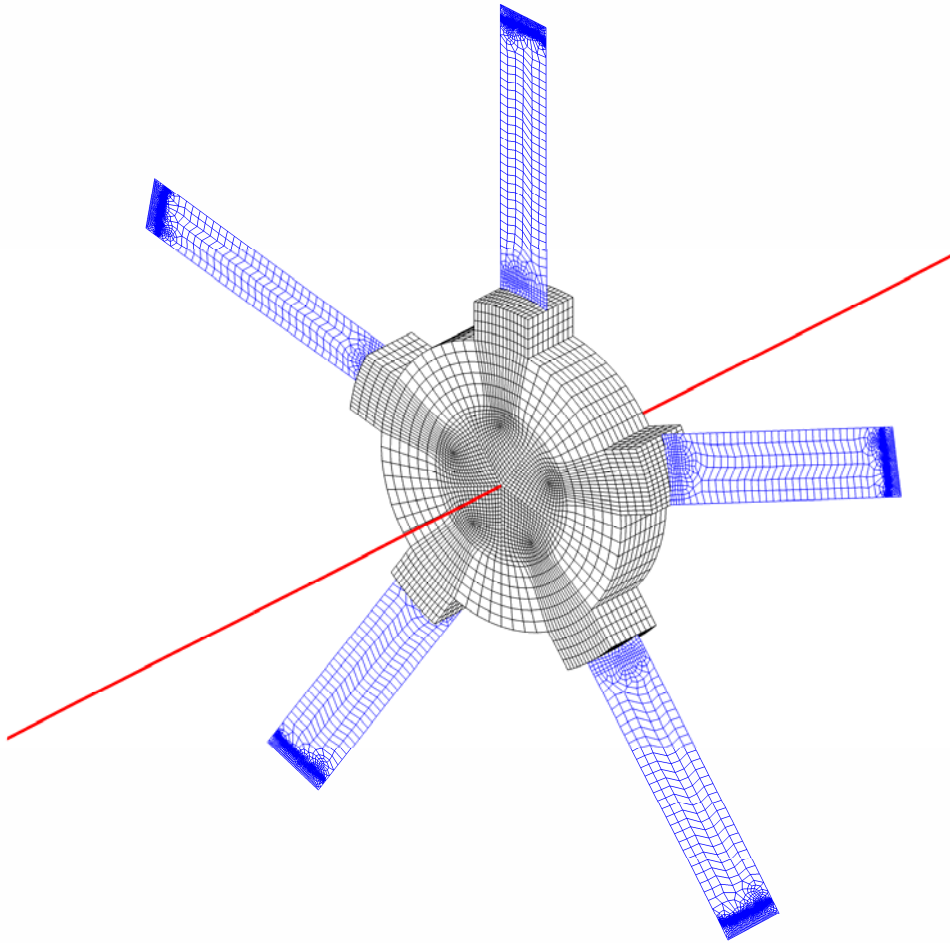
Figure 52: Finite element model

The pulses exerted on each blade by the air-jet nozzle during rotation were approximated with a concentrated force on each blade. It was assumed that these forces were directly proportional to the respective pressure signals measured. For each blade number b, a normalized force F_b was approximated from the corresponding average pressure pulse waveform P_b:

$$F_b = \mu_b P_b$$

Equation 41

where μ_b normalizes each P_b with respect to P_1:

$$\mu_b = \frac{\max(P_b)}{\max(P_1)}$$

Equation 42

4.4.1 Model updating

Model updating of the FEM was conducted based on differences between FEM and experimental FRFs (Chapter 3). Optimization was performed with four sets of material properties consisting of the Young's modulus, Poisson ratio and density for each set. The four material property sets accommodated the optimization of the material properties of the rotor hub, the individual blade clamp interfaces, the shaft and the blades. The same material properties were used for all the blades while the individual blade thicknesses served as five additional optimization variables. Optimization was performed with the utilization of the Dynamic-Q Optimization Toolbox (Hay, 2002). FEM FRFs were calculated from Nastran eigenvalue analysis results (including residuals) in Matlab using modal decomposition (Pruemont, 2002:21). Following the updating of the FEM material properties, the modal damping parameters were updated in a similar way. The FRFs of the updated FEM are compared with the experimental FRFs in Figure 53, showing very good correlation.
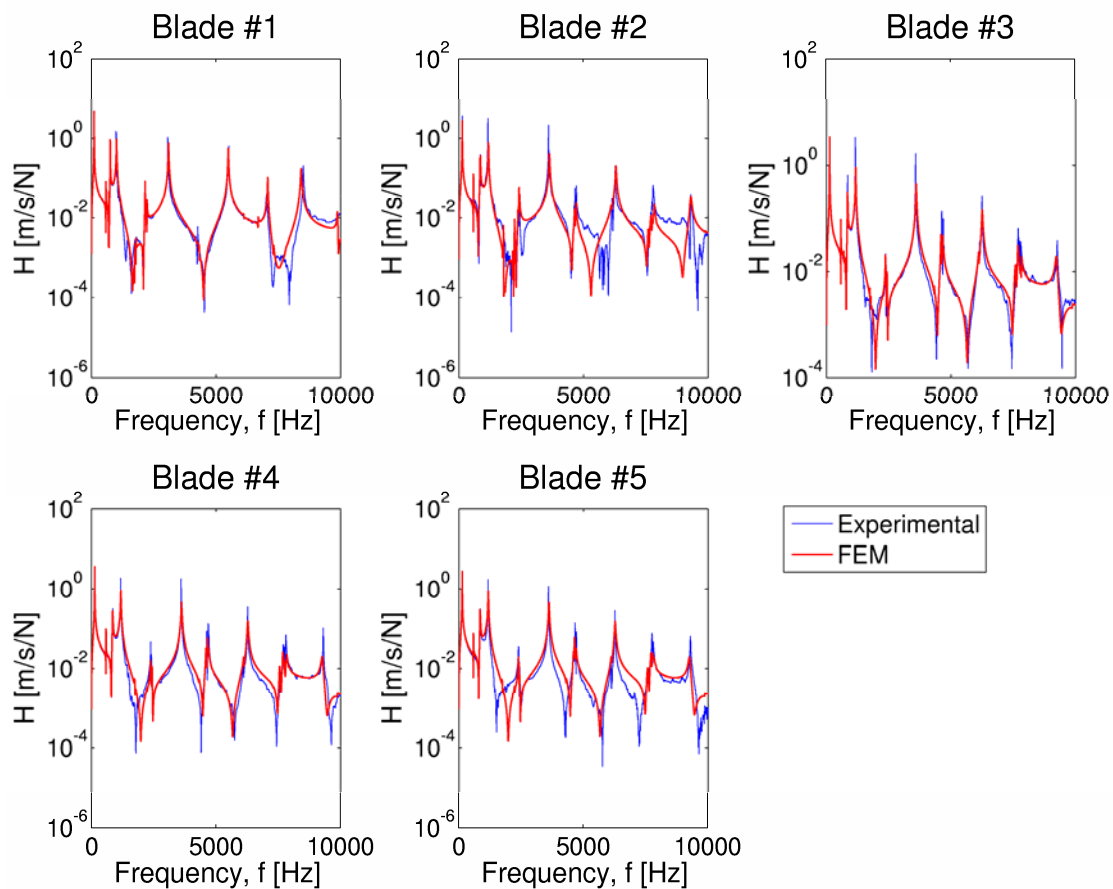

Figure 53: Updated FEM FRFs

4.4.2 TLDV simulation

TLDV was simulated in the FEM by applying F_b (Equation 41) in succession so that the peak occurrences of each F_b corresponded with that of the measured P_b signals. This is depicted in terms of rotor angle in Figure 54, with F_b obtained from P_b measured at 720 RPM. It was assumed that the F_b waveforms remained unchanged in the angular domain at the various rotor speeds and damage cases. The significant variation in the peak amplitudes of F_b shows a correlation with the variation in the blade-nozzle standoff distances measured in the test rotor blades.
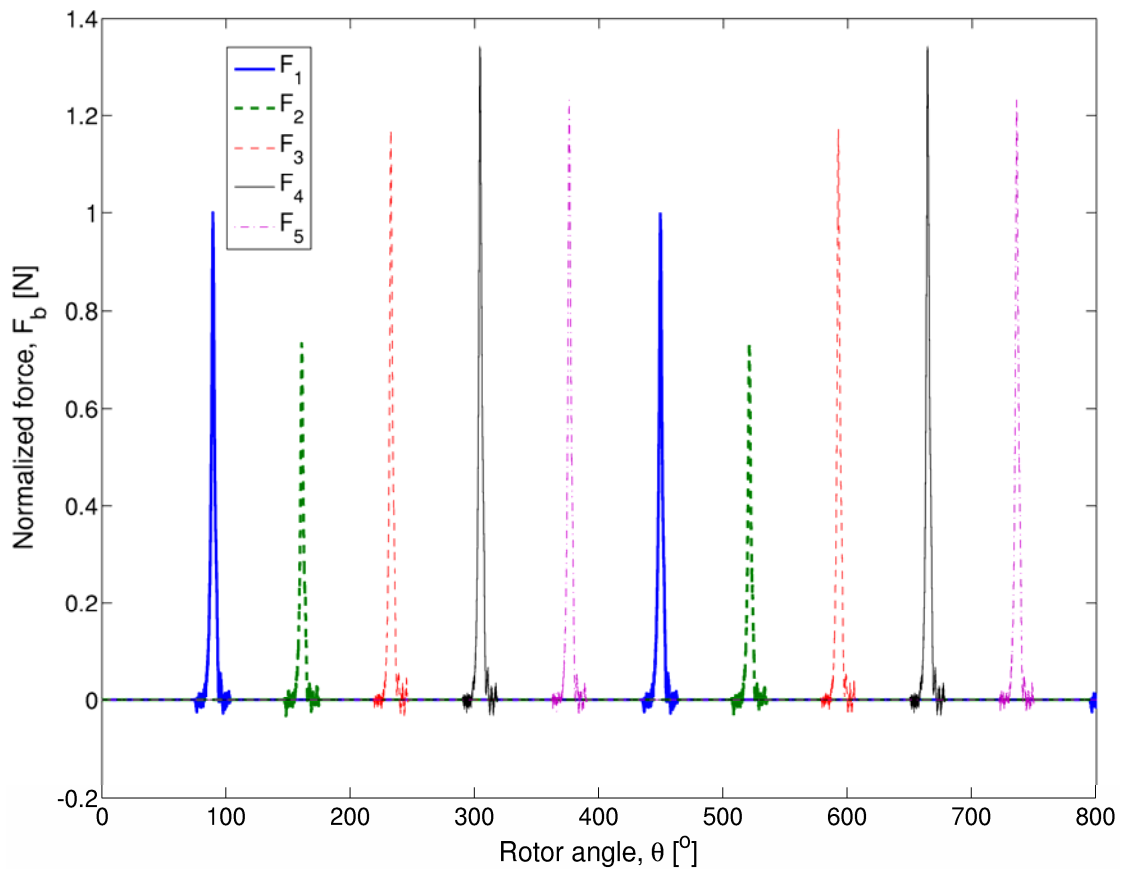

Figure 54: FEM force functions

Using initial conditions of rest, pulses were applied to the FEM over a period corresponding to 14 revolutions to allow for the development of steady-state vibration. TLDV measurements were then simulated using the FEM for the different damage levels and rotor speeds considered during experimental testing. Figure 55 depicts a comparison of the TLDV velocity results (v_L) of numerical simulations for damage cases 0-15 with the experimental measurements for blade #1, showing a close correlation. An additional damage case XVI was considered in the FEM corresponding to a blade #1 damage level of 16.7 mm.
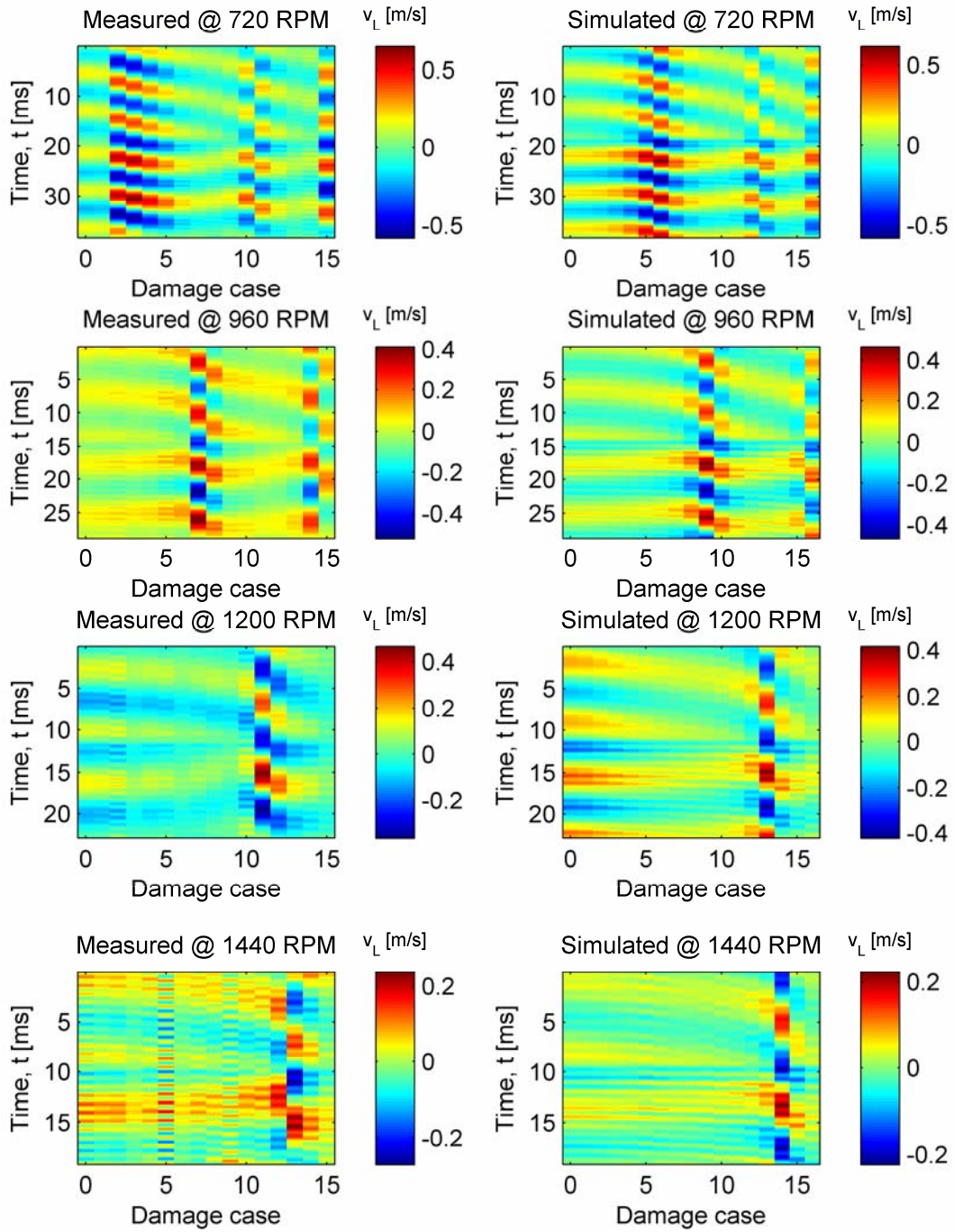
Figure 55: Time response comparison for different damage levels

At various damage cases, high response amplitudes are observed along with large phase angle changes (as can be seen from the distinct discontinuities in velocity pattern at these damage cases), e.g. the measurements for damage cases 7 and 14 at

960 RPM. This correlates with similar observations made in Section 3.3 for a single blade. To study this phenomenon, the change in the FEM first bending-mode natural frequency ω_1 of blade #1 with an increasing damage level is superimposed on various orders of the different rotor speeds in Figure 56. It can be seen from this figure that ω_1 coincides with rotor orders at damage levels in accordance with the discontinuities noted in Figure 55.
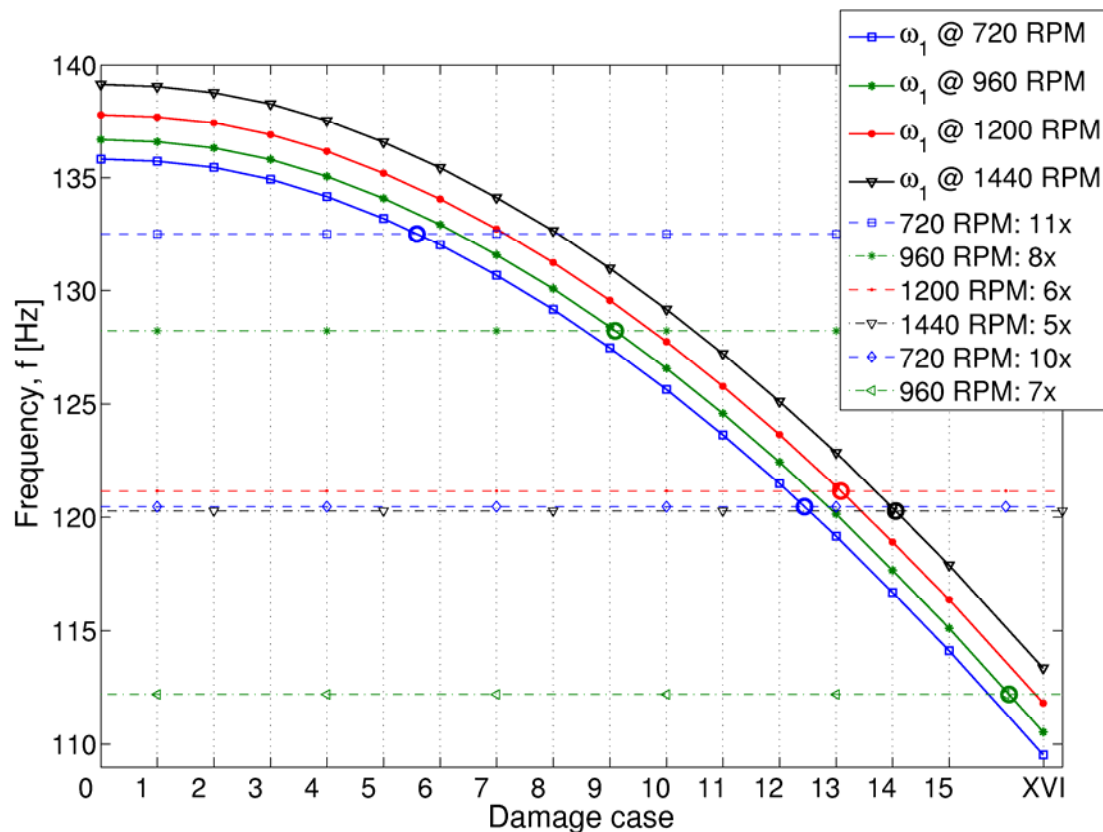

Figure 56: FEM blade #1 ω_1 comparison with rotor orders

Evaluating the velocity RMS values of the simulated results, the coinciding of high velocity response with rotor orders at the relevant damage levels are clearly demonstrated in Figure 57. It is furthermore clear from this figure that RMS holds promise as a parameter for blade condition monitoring: Not only is a systematic change in RMS value indicative of deterioration in blade health, but it can also be seen that if a sign change occurs in the RMS trend slope, ω_1 is close to a rotor order. Thus RMS can serve as an indicator of blade natural frequency shift at a fixed rotor speed on the condition that the blade loading and operational conditions remain constant. This observation also indicates that run-up and run-down ELDV records of the rotor blades along with the rotor speed are valuable for estimating the individual ω_1 values.
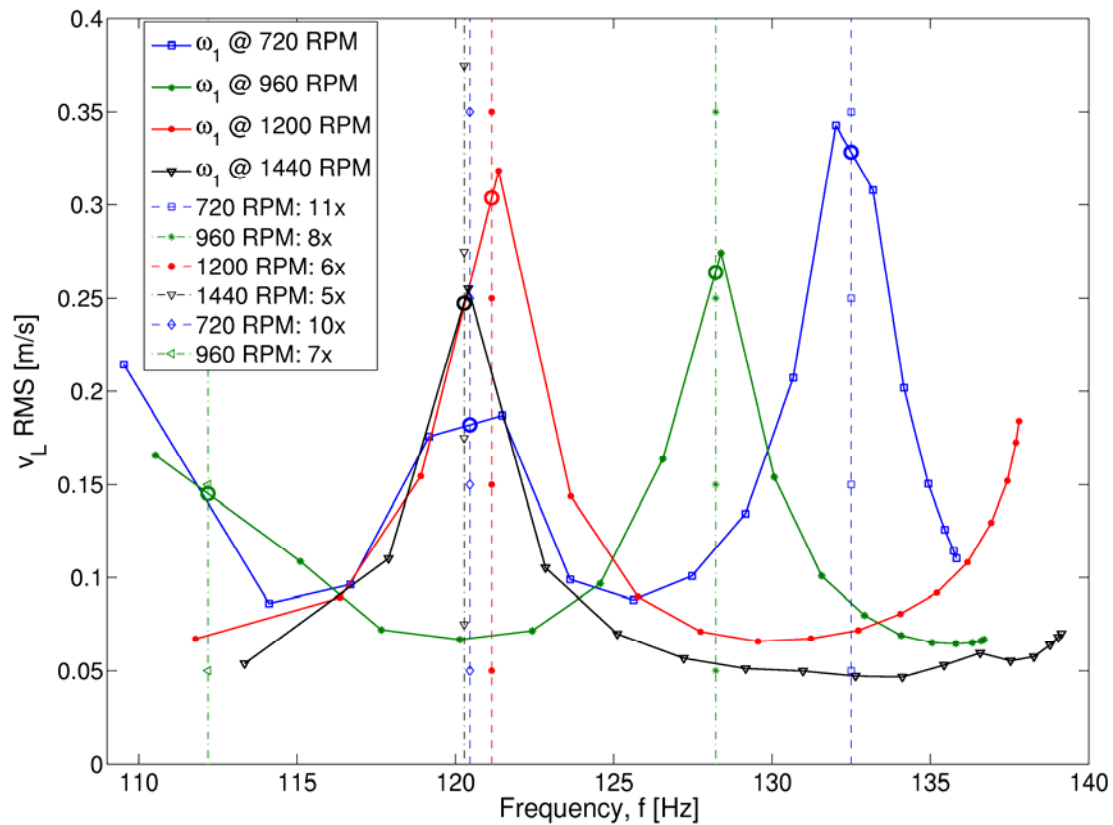
Figure 57: Blade #1 simulated RMS values as functions of FEM blade #1 ω_1

4.5 Experimental results

4.5.1 MAUPAT analysis

In Chapter 3, NHFA was performed on ELDV signals to obtain MAUPATs over ranges within 5% of the individual natural frequencies of the single blade. Due to blade mistuning and the effect of global mode shapes, groupings of mode shapes at various frequencies were present in the multi-blade test rotor. As a result, NHFA was performed in this chapter to obtain MAUPATs over ranges around the average of the blade natural frequency groupings. The individual ranges were determined from the variation around each reference frequency. The reference frequencies considered are listed in Table 6 along with the relevant ranges.

When evaluating the experimental MAUPAT results, it soon became apparent that interpreting the trends is more complicated on a multi-blade rotor than on the single-blade rotor used in Chapter 3. This is demonstrated in Figure 58 for the MAUPATs of damage cases 0-15 around f_1.

Table 6: MAUPAT reference frequencies

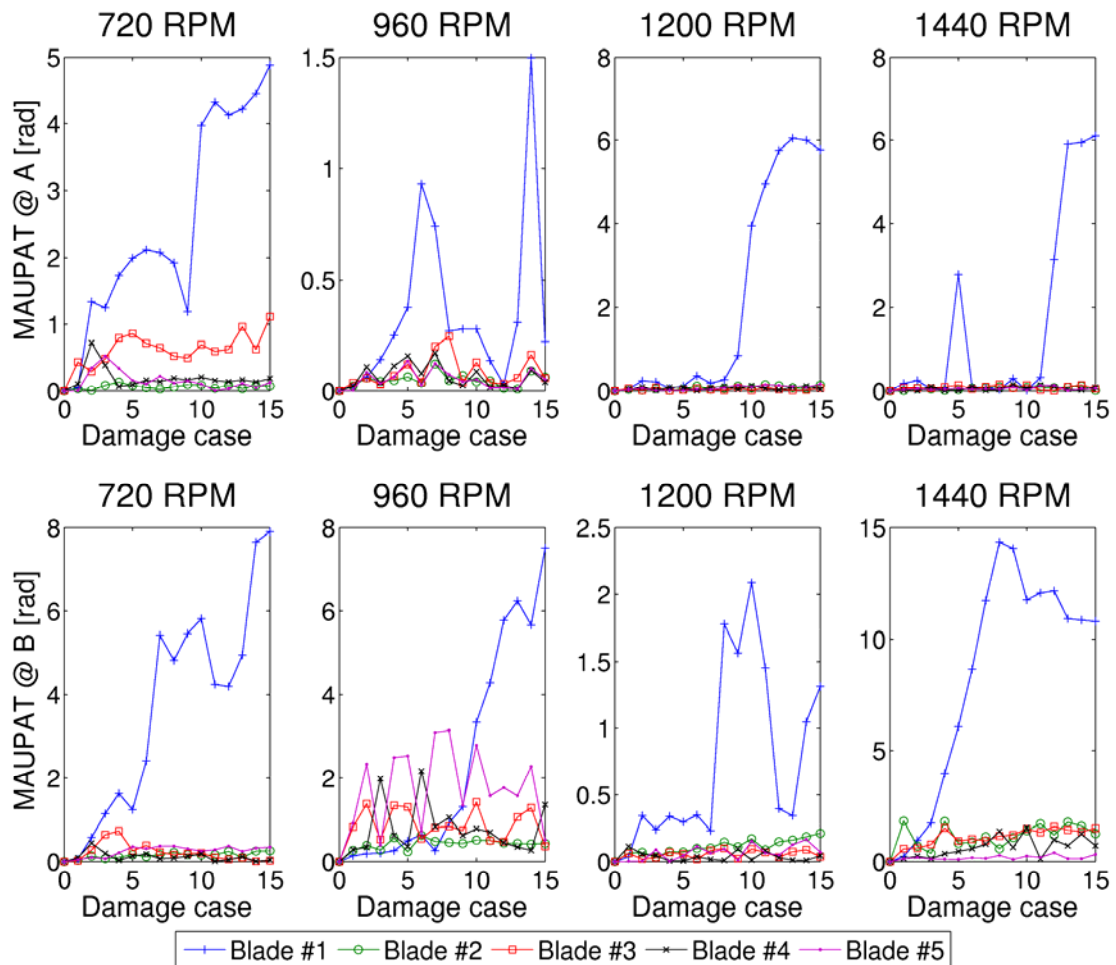| Reference number	Reference frequency, f_{ref} [Hz]	Frequency range [Hz]
1	135	±5
2	600	±50
3	865	±25
4	1167.5	±12.5
5	2390	±50
6	3590	±20
7	4600	±40
8	6260	±30
9	7750	±150
10	9270	±50

Figure 58: Damage cases 0-15 MAUPATs around f_1

This figure shows a number of blade #1 trend jumps, corresponding with the observations from Figure 55 relating to the proximity of blade #1 ω_1 and rotor order. Secondly, it is clear that ELDV measurement position (A or B) has a definite effect on the trends. It also is evident that depending on rotor speed and measurement position, it may prove difficult to identify the damaged blade. This is either due to a lack of a strong and consistent trend in the damaged blade MAUPATs (e.g. position A at 1440 RPM) or large changes in the MAUPATs of some undamaged blades (e.g. position B at 960 RPM). The trends of blade #1 furthermore do not always increase monotonically with damage.

In order to distinguish between damaged and undamaged blades, it was necessary to evaluate the statistical properties of the individual blade trends. After evaluating various statistical parameters, the trend standard deviation (σ) was found to yield the most favourable results. Figure 59 depicts the σ trends of the MAUPATs (σ_{MAUPAT}) around f_1, showing improvement in trend separation in most cases. However, strong trends are still visible in undamaged blades in some cases (e.g. position B at 960 RPM).
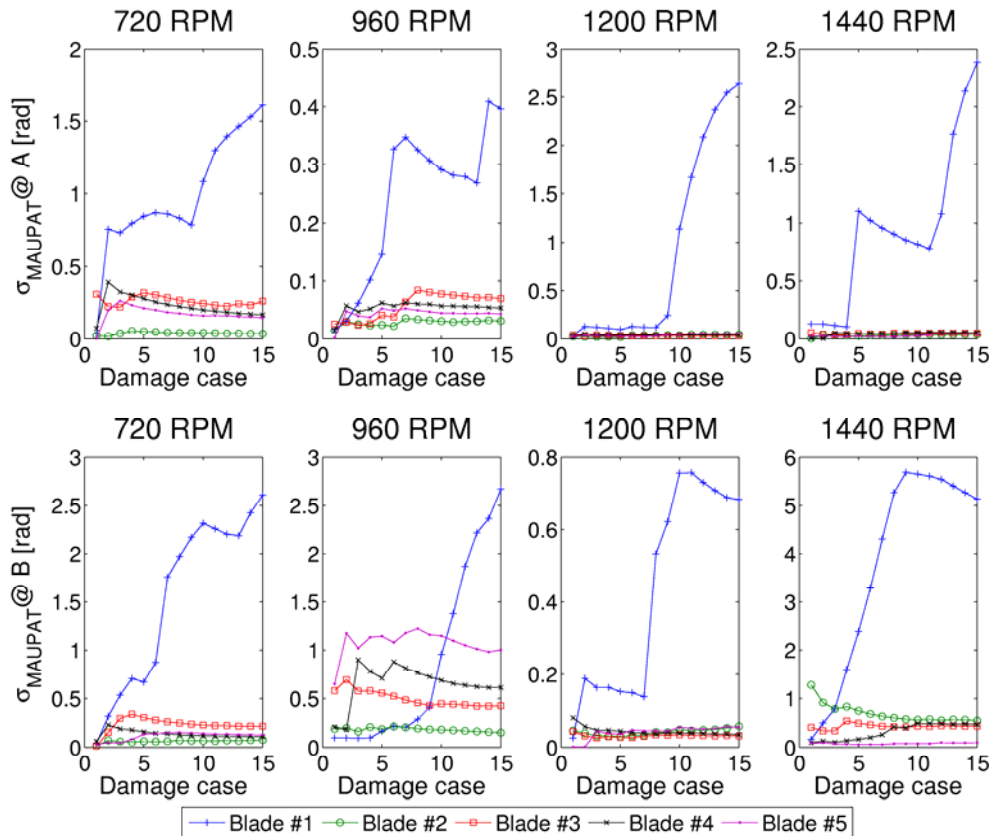

Figure 59: Damage cases 0-15 σ_{MAUPAT} trends around f_1

To obtain more robust results, the averages of the σ_{MAUPAT} trends ($\tilde{\sigma}_{MAUPAT}$) around the remaining f_Rs were calculated after normalization. The outcome is depicted in Figure 60 and it is noted that definite improvement is yielded where trend separation proved to be difficult previously (e.g. position A at 1200 RPM, position B at 960 RPM).
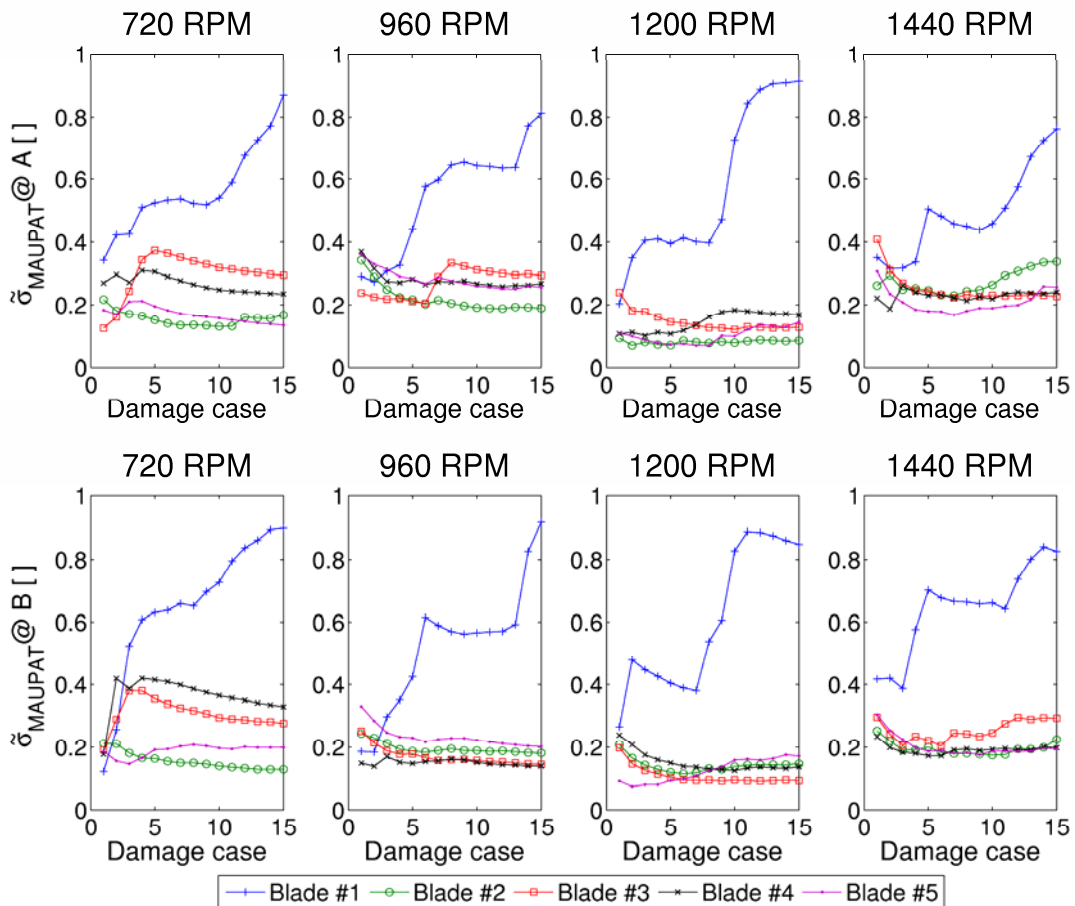

Figure 60: Damage cases 0-15 $\tilde{\sigma}_{MAUPAT}$ trends

The improvements in average trend separation of blade #1 from using σ_{MAUPAT} (Figure 59) and $\tilde{\sigma}_{MAUPAT}$ (Figure 60) are presented in Table 7 relative to the MAUPAT separation around f_1 (Figure 58). It is clear that at various instances, σ_{MAUPAT} trends yield improvement whereas $\tilde{\sigma}_{MAUPAT}$ trends yield deterioration in trend separation, and *vice versa*. Thus the choice of trend for damage detection purposes should receive some consideration, and it may be useful to use the trends in conjunction.

Table 7: Blade #1 trend separation improvement for damage cases 0-15

Rotor speed [RPM]	Trend separation improvement [%]			
	σ_{MAUPAT} @ A	$\tilde{\sigma}_{MAUPAT}$ @ A	σ_{MAUPAT} @ B	$\tilde{\sigma}_{MAUPAT}$ @ B
720	11.62	-23.88	23.89	-7.74
960	149.43	51.64	-44.63	79.89
1200	-6.25	30.57	60.29	47.93
1440	53.83	0.12	15.81	-15.85

When this approach is applied to the measurements of damage cases 16-30, Figure 61 is obtained showing the applicability of the technique when multiple blades are damaged.

To investigate whether further improvement on the trends could be obtained via frequency component isolation prior to NHFA analysis, finite-duration impulse response (FIR) filtering and Vold-Kalman filtering were applied to the signals. However no significant improvement was obtained in the results.
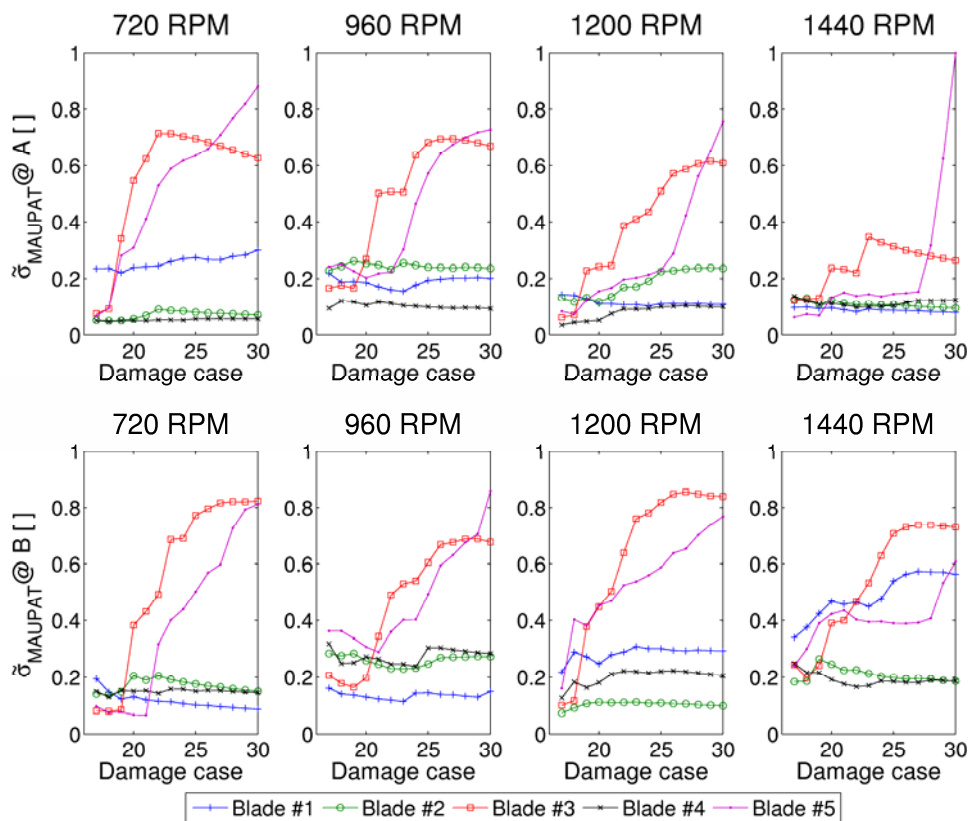

Figure 61: Damage cases 16-30 $\tilde{\sigma}_{MAUPAT}$ trends

4.5.2 Time domain analysis

Various time domain parameters were evaluated namely crest factor, kurtosis, variance, covariance (Norton and Karczub, 2003). Of these RMS and correlation coefficient yielded the best results. Figure 62 and Figure 63 depict the RMS standard deviation trends (σ_{RMS}) for damage cases 0-15 and those of damage cases 16-30 respectively. In general, good results are obtained for all the damage cases except for the lower damage cases at position A at 960 RPM and 1200 RPM. The σ_{RMS} results obtained at position B at 720 RPM for blade #4 erroneously show a strong trend for damage cases 0-15 (Figure 62). As seen from Figure 63, trend separation is poor at 1440 RPM at both measurement locations for damage cases 16-28.

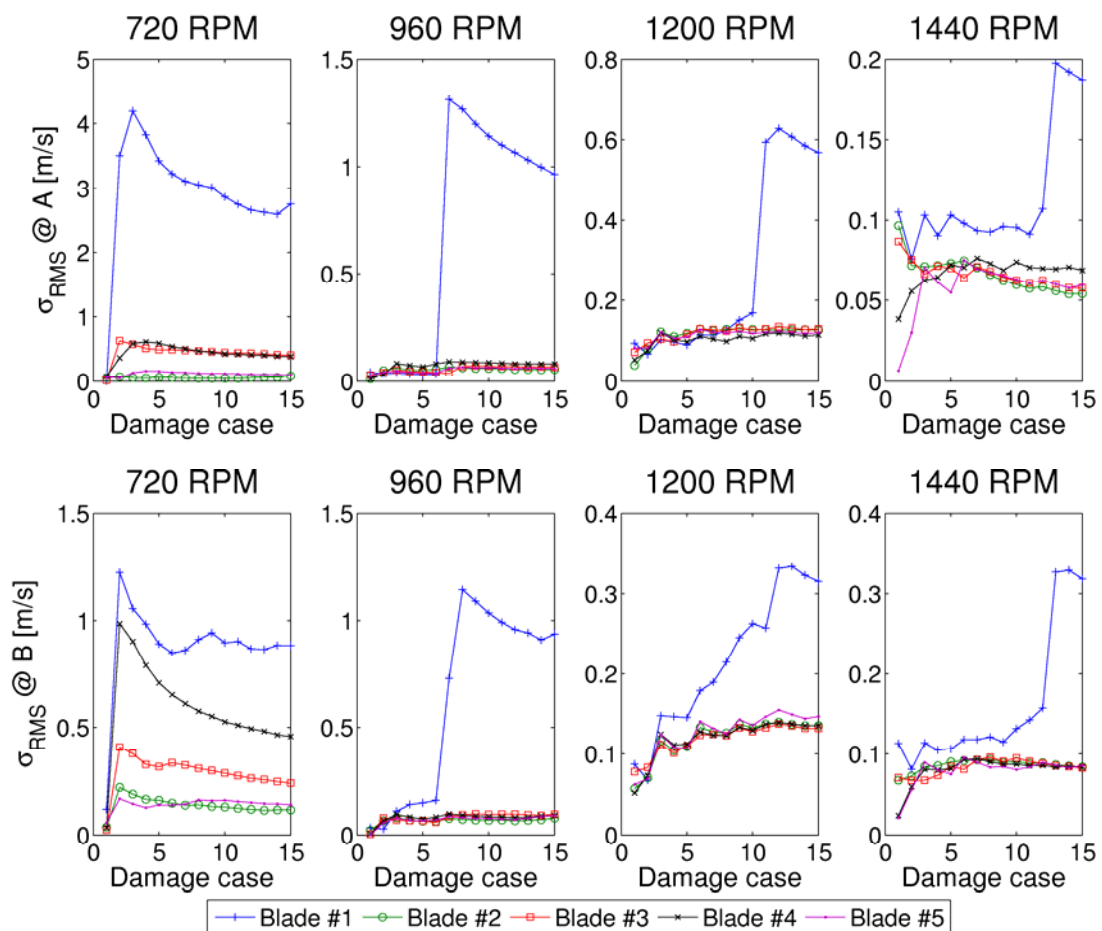**Figure 62: Damage cases 0-15 σ_{RMS} trends**

The trends of correlation coefficient standard deviation (σ_{CORR}) are considered in Figure 64 and Figure 65 for damage cases 0-15 and 16-30 respectively. Again good results are generally obtained for all damage cases.
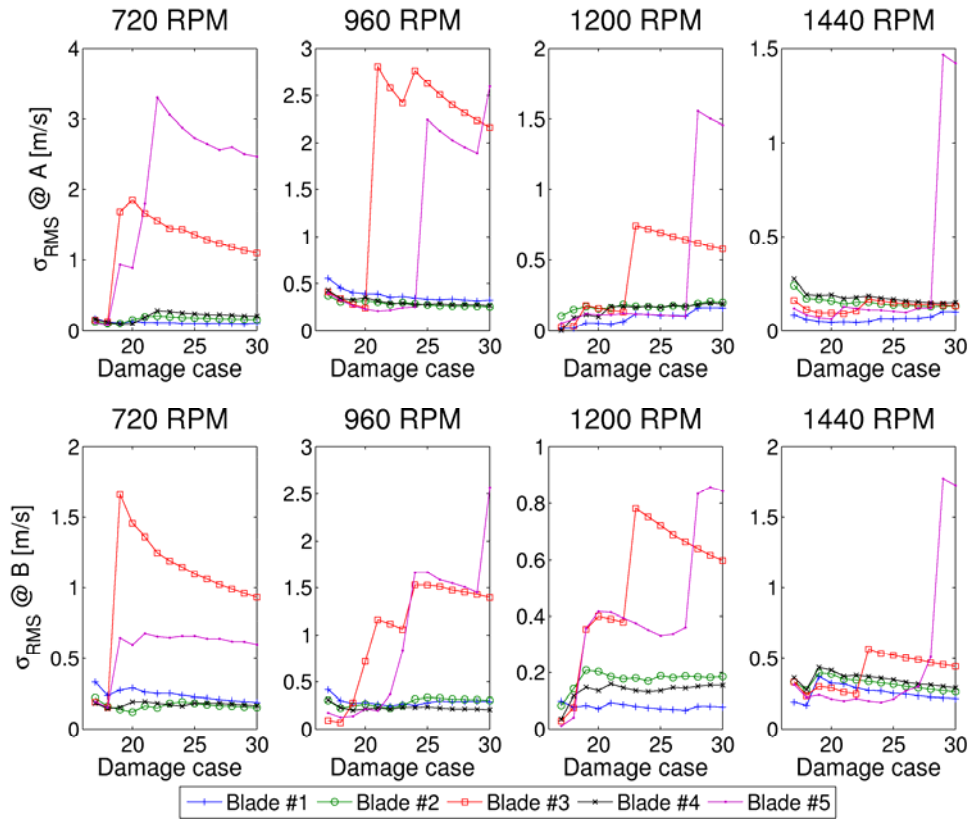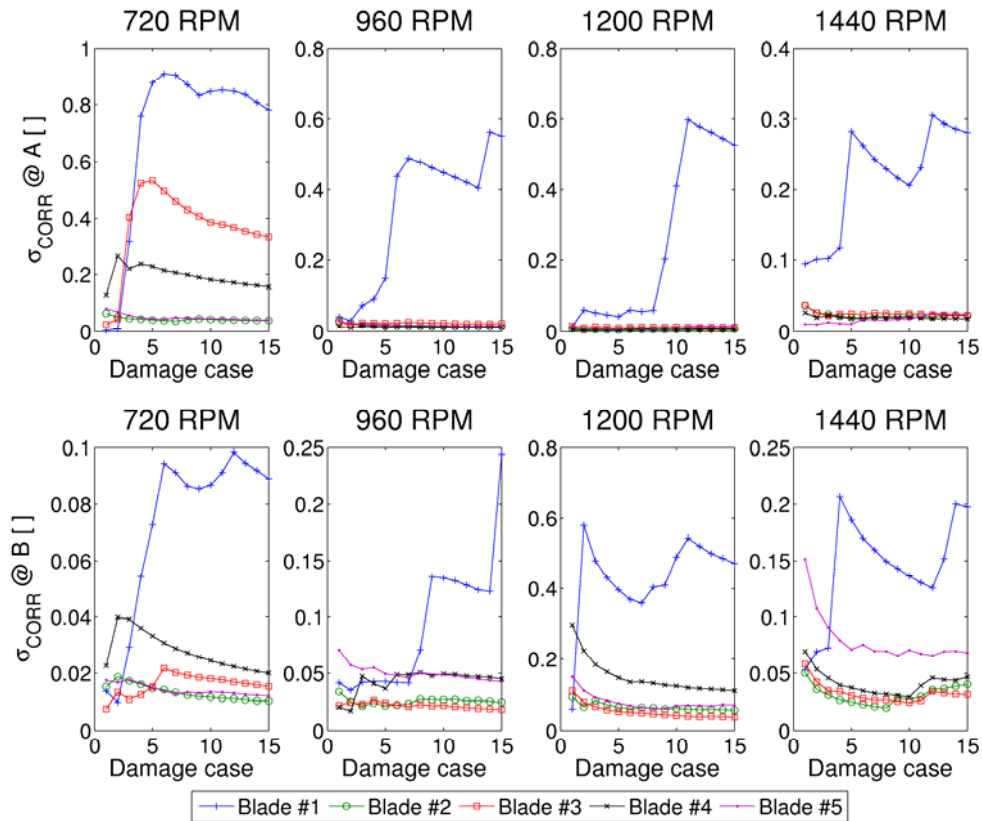
Figure 63: Damage cases 16-30 σ_{RMS} trends

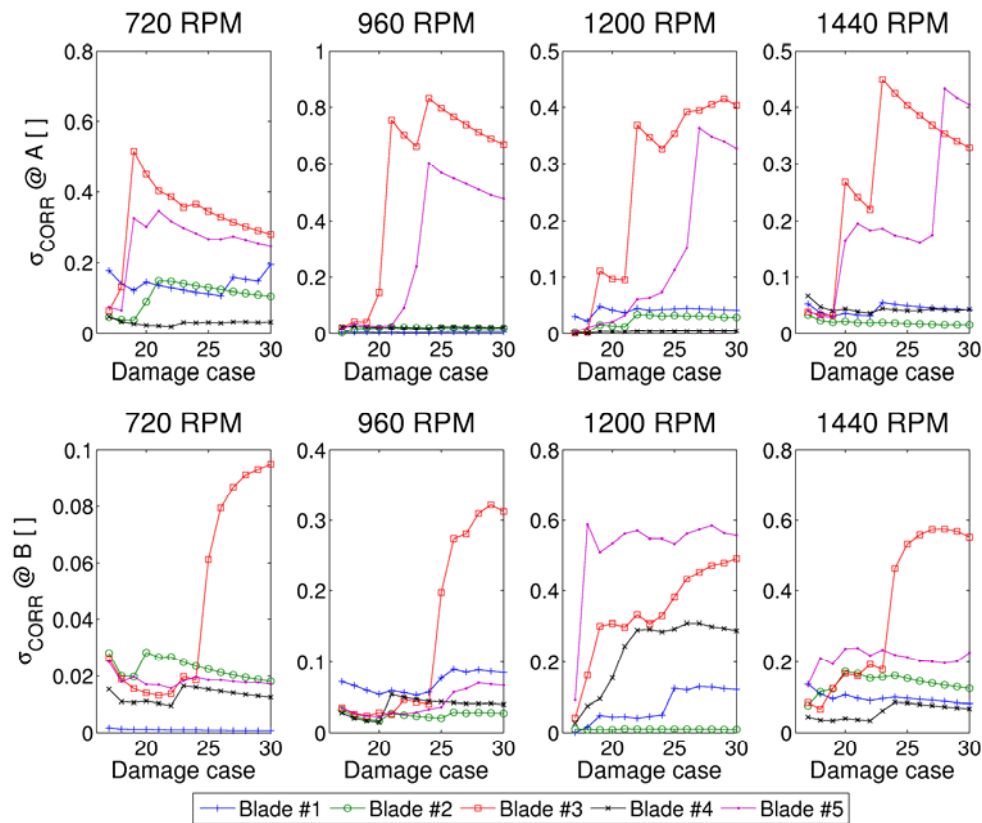**Figure 64: Damage cases 0-15 σ_{CORR} trends**

Figure 65: Damage cases 16-30 σ_{CORR} trends

An erroneous trend is visible at damage cases 0-15 for blade #3 at position A at 720 RPM (Figure 64). Blade #4 also exhibits strong trends at 720 RPM at both measurement locations for damage cases 0-15. In Figure 65 good results are obtained at position A whereas weak trends are visible for blade #5 at position B except at 1200 RPM. However at position B, a strong σ_{CORR} trend for blade #4 is erroneously indicated at 1200 RPM. Also at both measurement locations, strong erroneous trends for blade #2 are visible at 720 RPM.

4.5.3 ANN implementation

It is evident from the results obtained for $\tilde{\sigma}_{MAUPAT}$, σ_{RMS} and σ_{CORR} that the different parameters need to be considered in conjunction to identify and quantify blade damage accurately. In addition, it is clear that the parameters from multiple ELDV measurement positions are advantageous to this purpose. One approach to efficiently harvesting the information from the diverse parameters is to employ ANNs.

Using an architecture consisting of two layers, one with 14 neurons and the other with a single neuron, a separate ANN was trained for each rotor speed. Tan-Sigmoid transfer functions were used for all the neurons.

Ten different sets of parameters were extracted for each blade from the average of ten ELDV samples for each damage case and rotor speed. Each set consisted of seven parameters, namely $\tilde{\sigma}_{MAUPAT}$ at position A and B, σ_{RMS} at position A and B, σ_{CORR} at position A and B as well as the blade number b. Each network was then trained to yield the blade-specific damage level D_b. A schematic diagram of the ANN architecture is presented in Figure 66.

Input layer
(14 neurons)

Output layer
(1 neuron)

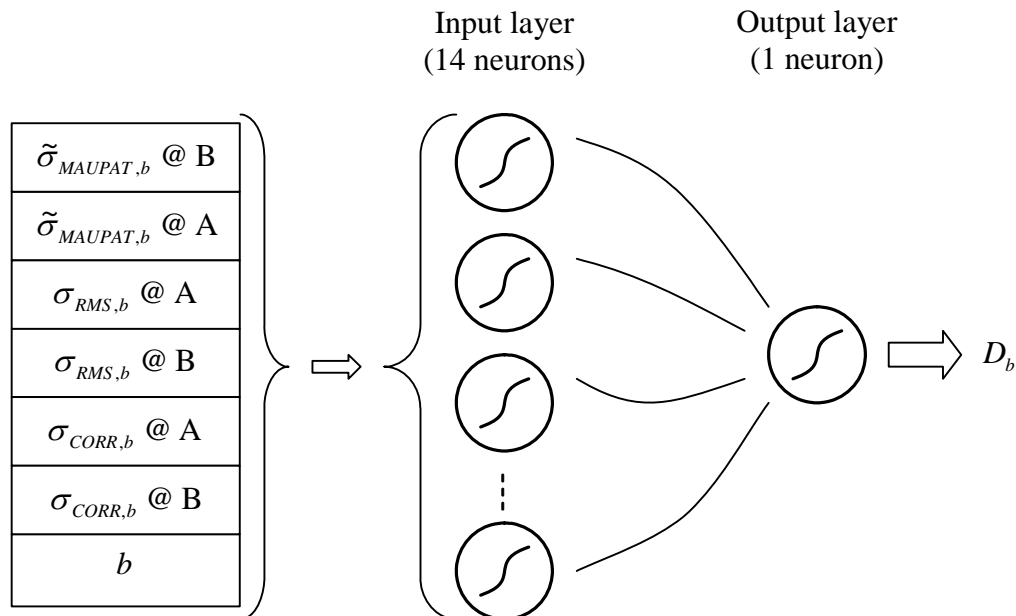| |
|---|
| $\tilde{\sigma}_{MAUPAT,b}$ @ B |
| $\tilde{\sigma}_{MAUPAT,b}$ @ A |
| $\sigma_{RMS,b}$ @ A |
| $\sigma_{RMS,b}$ @ B |
| $\sigma_{CORR,b}$ @ A |
| $\sigma_{CORR,b}$ @ B |
| b |

D_b

Figure 66: ANN architecture

Following training with eight sets of parameters, each ANN was evaluated with the two remaining sets and the average results are depicted in Figure 67 with the dashed lines representing the ANN training targets. Good results are observed from this figure, showing the ANNs to be capable of both identifying and quantifying blade damage.
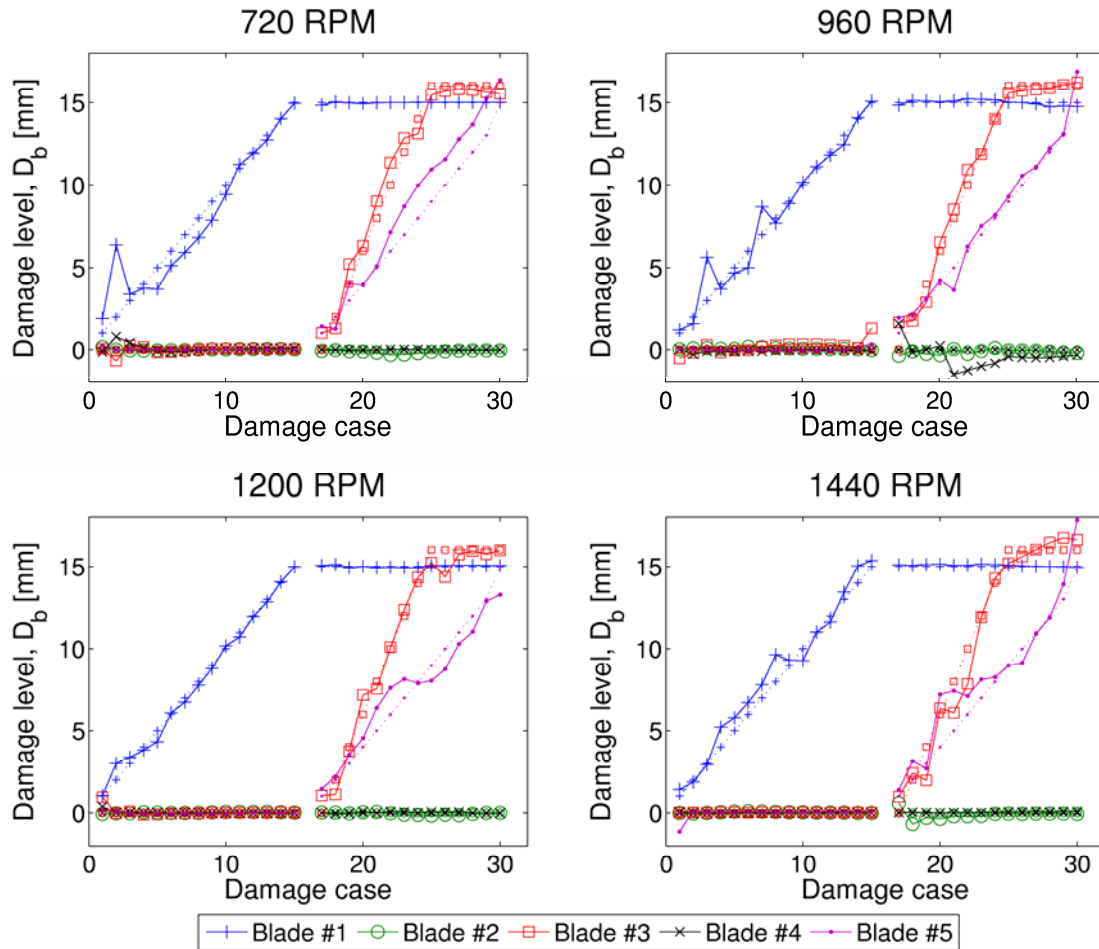
Figure 67: ANN results

4.5.4 Natural frequency estimation

The results presented in Section 4.5.1 to 4.5.3 are useful for identifying and quantifying blade damage relative to a reference point. In order to obtain that reference point, it would be most useful to know the natural frequencies of each individual blade. Although these frequencies can be obtained via offline FRF testing, this approach requires long downtimes and can typically be performed only during outages. It is therefore desirable to estimate the frequencies in an on-line fashion.

In Section 4.4.2 it was shown numerically that ω_1 can be estimated for each blade from run-up and run-down ELDV records. To validate this, ELDV measurements were taken on the test rotor at position A during run-up and run-down events over rotor speeds ranging from 340 RPM to 1440 RPM. The RMS trend of the ELDV run-down signatures of blade #1 at position A is given in Figure 68 for damage case 30, showing a number of peaks.
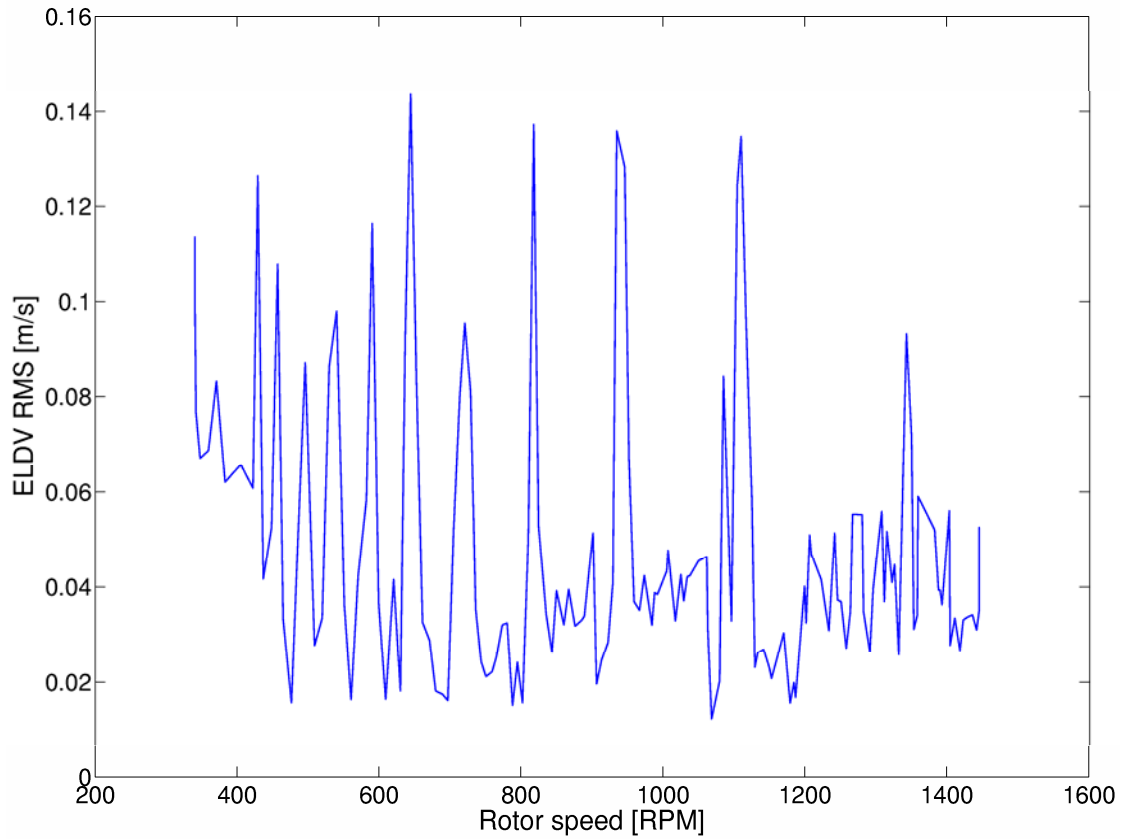
Figure 68: Blade #1 run-down ELDV RMS signature

Consider a vector $\overline{\Psi}$ containing the rotational frequencies ψ in descending order at the predominant peaks:

$$\overline{\Psi} = [\psi_1, \psi_2, ..., \psi_J]$$

Equation 43

with $\psi_1 > \psi_2 > ... > \psi_J$ and J is the number of peaks considered.

Since the rotor speed changes and since it can be assumed that ω_1 of each blade remains constant during a run-up or run-down, the rotor order number at each successive RMS peak needs to be incremented. If a vector $\overline{\varepsilon}$ consisting of the rotor order numbers at the RMS peaks is defined as

$$\overline{\varepsilon} = \delta + [1, 2, ..., J]$$

Equation 44

with δ an integer constant, a vector $\overline{\omega}$ can be constructed with elements approximating ω_1 by multiplying the elements of $\overline{\Psi}$ and $\overline{\varepsilon}$:

109

$$\overline{\omega} = \left[\overline{\varepsilon}_1\overline{\Psi}_1, \ \overline{\varepsilon}_2\overline{\Psi}_2, \ ..., \ \overline{\varepsilon}_J\overline{\Psi}_J\right]$$

Equation 45

By selecting δ so that the standard deviation of $\overline{\omega}$ is minimized, an estimate of ω_1 can be obtained from the mean of $\overline{\omega}$:

$$\omega_{1,est} = \frac{\overline{\varepsilon} \cdot \overline{\Psi}}{J}$$

Equation 46

Using the results from both a run-up and run-down signature, the average $\omega_{1,est}$ results are listed in Table 8 showing good correlation with the natural frequencies obtained from modal testing on the stationary rotor.

Table 8: Natural frequency estimation

b	FRF frequency [Hz]	$\omega_{1,est}$ [Hz]	% error
1	106.25	109.48	3.04
2	137.5	138.11	0.44
3	103.125	105.04	1.89
4	137.5	138.34	0.61
5	109.375	111.64	2.07

If the machine is operated in such a way that run-up and run-down events occur regularly, $\omega_{1,est}$ can be used as an additional ANN parameter.

4.6 Measurement uncertainty sensitivity analysis

To determine the effects of laser misalignment and speckle noise on the MAUPAT and time domain results, a sensitivity analysis was conducted on the signal processing techniques used in this chapter. In order to obtain a representative speckle noise signal experimentally, ELDV measurements were recorded on the blades in the absence of nozzle excitation. The same opto-reflective material used for the measurements of Section 3.3 and Section 4.5 was utilized again and a typical signal measured at 720 RPM is presented in Figure 69. From this figure, it is clear that the signal is dominated by noise. Since this signal was repeatable, it was readily assumed that noise is directly caused by the opto-reflective material's speckle pattern since speckle noise has a pseudo-random nature (Rothberg, 2006:4526). This signal was then used as part of the sensitivity analysis.
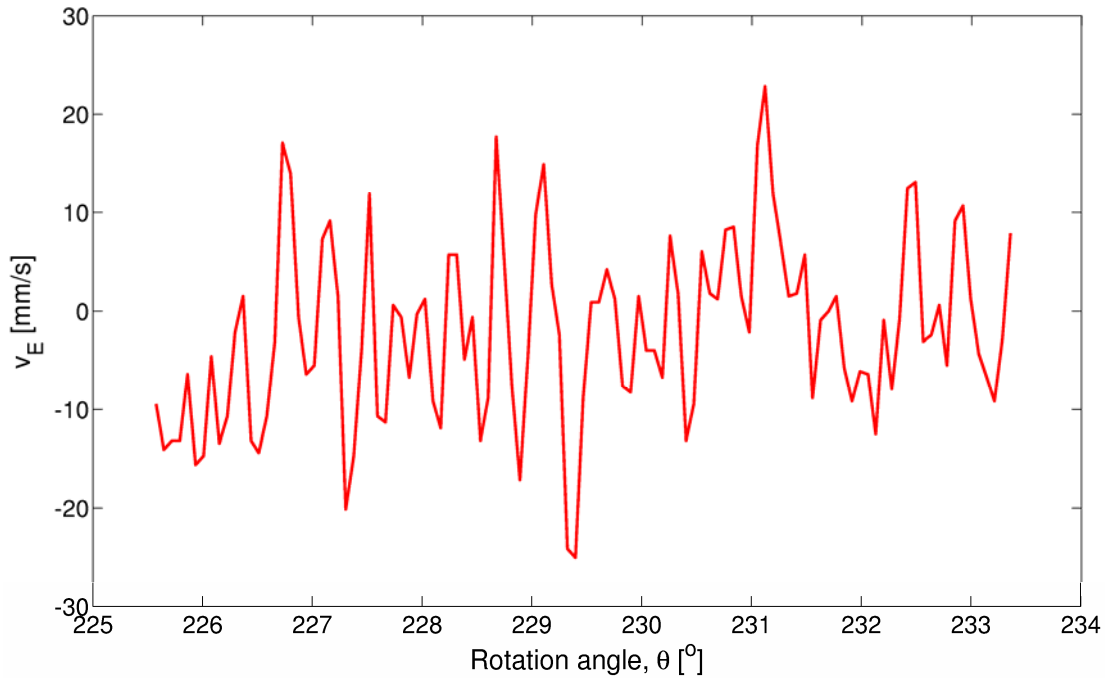
Figure 69: Speckle noise signal

The sensitivity analysis was conducted by adding noise to EVR signals simulated in the FEM at 720 RPM for damage cases 0-15. Six different cases were considered as listed in Table 9.

Table 9: Measurement uncertainty sensitivity analysis case matrix

Case #	Description
1	Stationary speckle noise signal
2	Speckle noise signal phase shift
3	Random speckle noise signals
4	Speckle noise signal frequency increase
5	$+0.227^o$ laser misalignment
6	-0.227^o laser misalignment

Case #1 involved adding the same speckle noise signal to each EVR signature, showing the direct effect of speckle noise presence on the results. With case #2, the same speckle noise signal was shifted 7 samples in time (corresponding to a 13.2^o phase angle shift) for each EVR signature to study the effects of systematic speckle noise phase shift on the results. For case #3, the FFT of the noise signal was calculated. Keeping the resulting FFT amplitudes unchanged, random phase angles were generated.

From these, inverse FFTs were calculated resulting in different speckle noise signals with the same frequency content, but with random time domain responses. A different speckle noise signal was then added to each EVR signature, showing the effects of random noise signal change on the results. Case #4 involved simulating a doubling in the speckle noise signal frequency by concatenating the same signal, and then resampling the resulting signal to obtain the original sample length. The same resampled noise signal was added to each EVR signature. Cases #5 and #6 simulated the effects of DC offsets in the ELDV measurements corresponding to a ±5 mm misalignment of the laser beam over the experimental standoff distance of 1.265 m (i.e. ±0.227^o misalignment).

4.6.1 MAUPAT results

The MAUPAT results of these simulations are represented in Figure 70 and Figure 71. The same reference frequencies and ranges listed in Table 6 were used during calculations. It is demonstrated that the addition of a static speckle noise signal affects the results in a limited way (Figure 70 b). However when the speckle noise signal itself changes for each damage case, the effects are more pronounced as seen in Figure 70 (c) and (d). Again in Figure 71 (b) as in Figure 70 (b), adding the same noise signal (in this case with twice the original noise signal frequency) has some effects on the results, though limited. Furthermore it is evident that the additions of DC components have clear effects on the results as demonstrated by Figure 71 (c) and (d). A positive DC component seems to increase the sensitivity of the results to damage whereas a negative DC component has the opposite effect.

When comparing the mean absolute MAUPAT errors for each analysis case over the range of damage levels considered, it becomes plain that results around the different f_{ref}s are affected differently by the different cases considered (Figure 72). In general, f_1 and f_2 are the least affected by the different disturbances whereas the higher f_{ref}s are more sensitive. Cases #2 and #3 (i.e. with dynamic speckle noise signals) yield roughly the same results with f_5, f_6, f_7 and f_9 affected the most by these. Overall does a positive DC offset (case #5) affect most of the f_{ref}s.
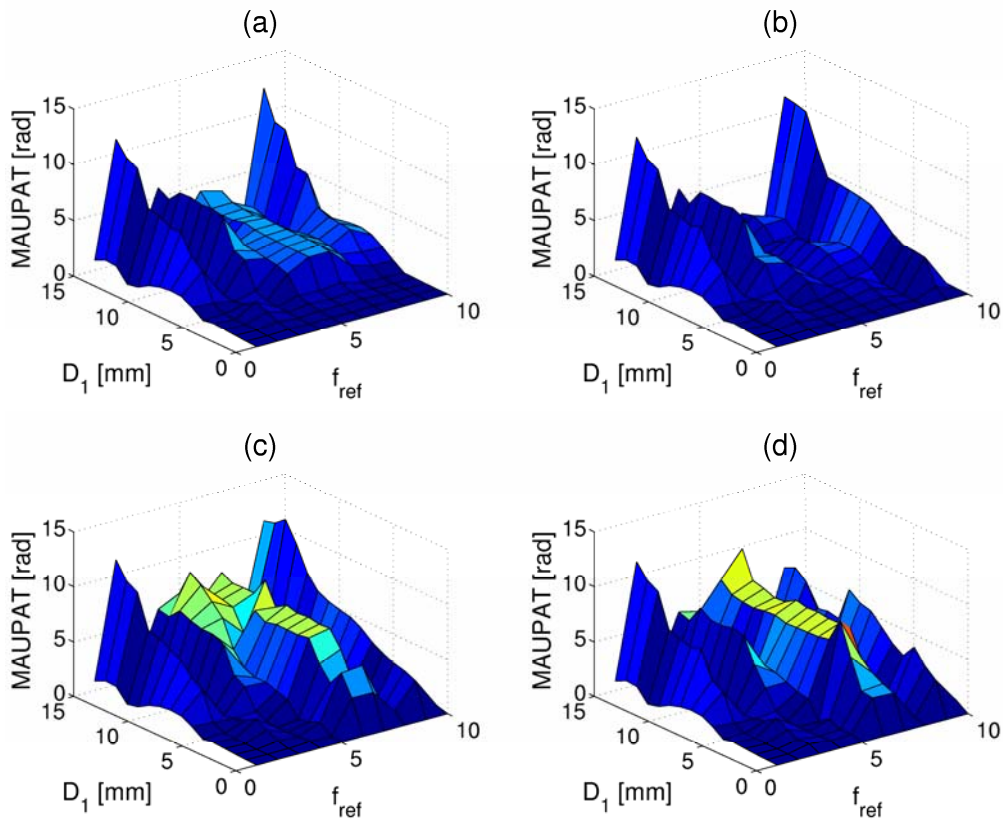
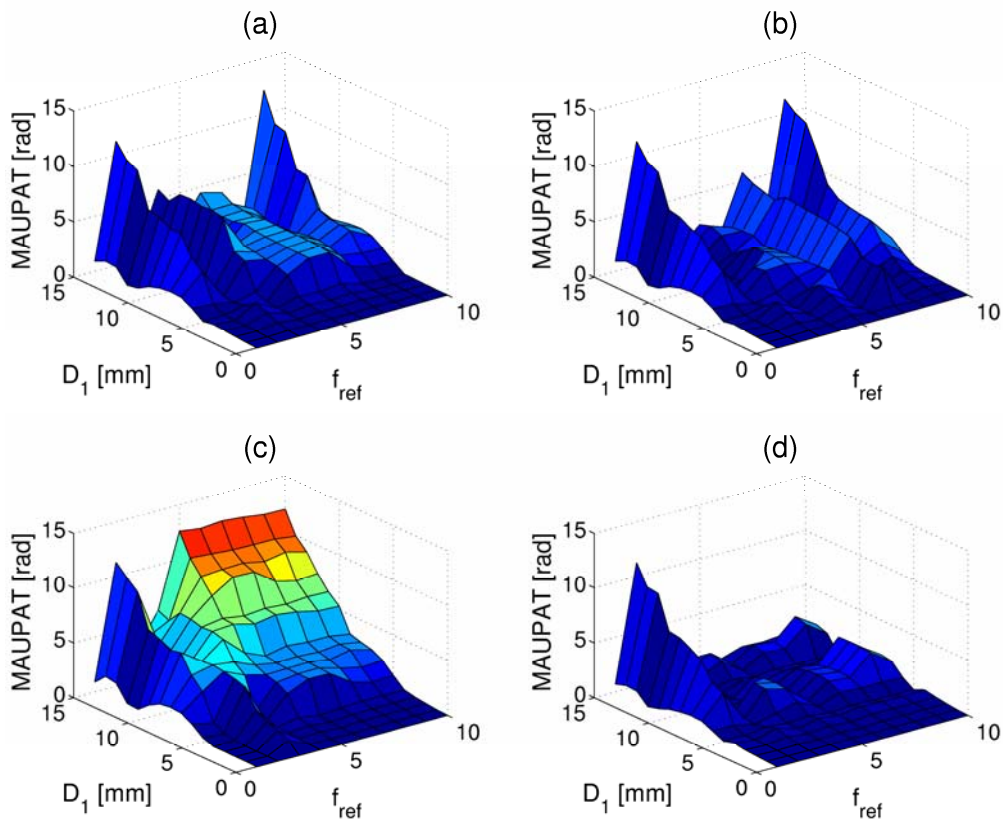**Figure 70: Sensitivity analysis MAUPAT results (a) Ideal (b) Case #1 (c) Case #2 (d) Case #3**

Figure 71: Sensitivity analysis MAUPAT results (a) Ideal (b) Case #4 (c) Case #5 (d) Case #6
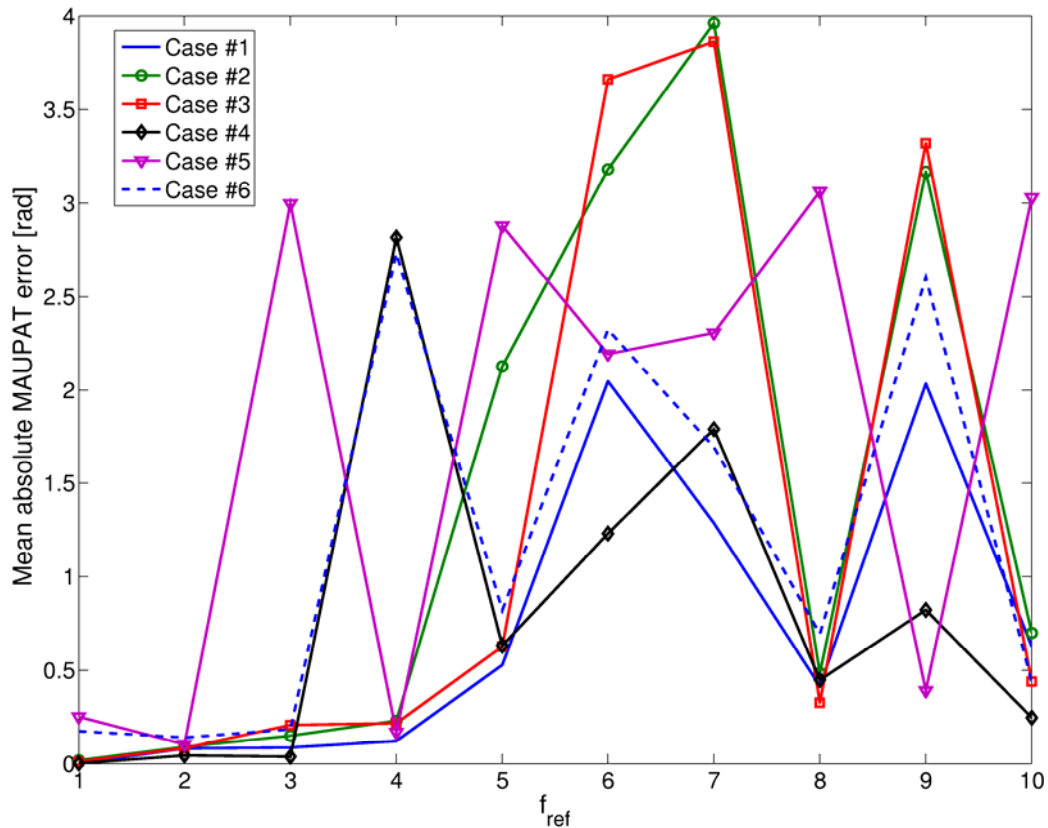
Figure 72: Mean absolute MAUPAT errors

4.6.2 Time domain results

The effects of the different sensitivity analysis cases were also studied on the time domain parameters considered in this chapter (i.e. RMS and correlation coefficient). The results are presented in Figure 73 in terms of mean absolute error.

RMS is affected only slightly for cases #1 to #4 whereas the introduction of DC offsets (cases #5 and #6) has pronounced affects on the RMS values. The opposite is observed for the correlation coefficient results.

4.6.3 Discussion

In the work presented in Chapter 3 and Chapter 4, it was assumed that the speckle noise signals were stationary for each blade for the duration of each damage level and rotor speed value. This assumption was valid since there were no changes (brought on by long term operational effects such as soiling) in the optical properties of the reflective material used during testing that had to be considered.
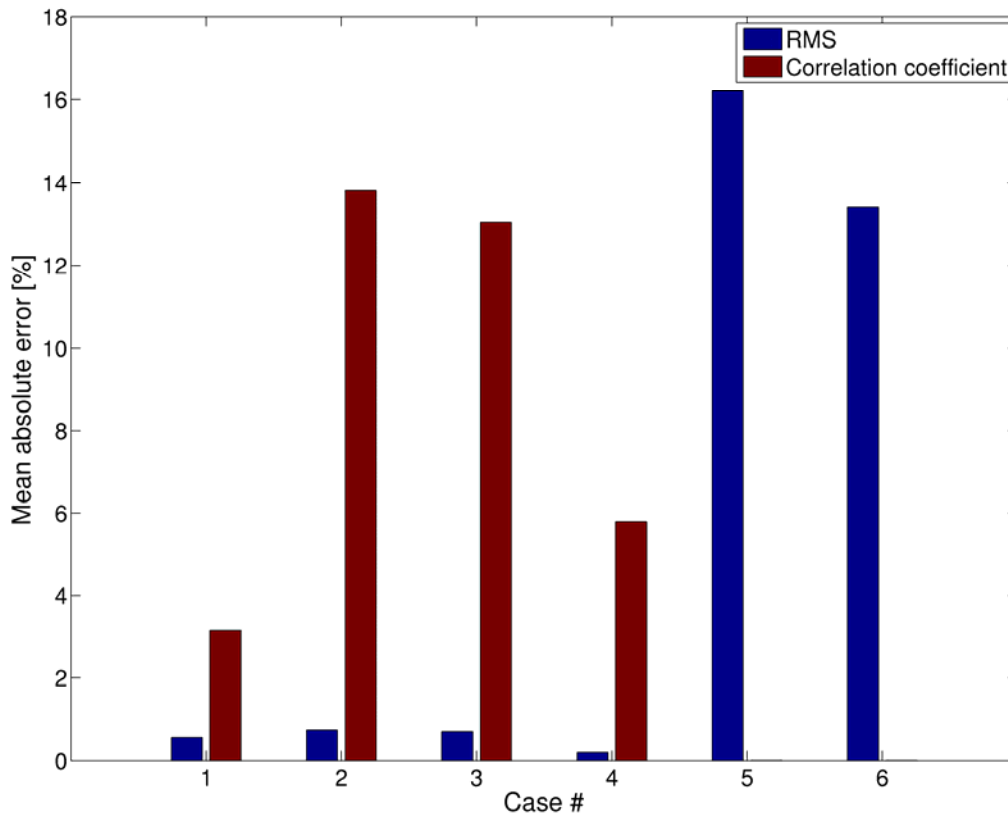
Figure 73: Mean absolute RMS and correlation coefficient errors

Furthermore no changes were made to the laser vibrometer orientation during testing, thus keeping the small misalignment effects constant during testing for each rotor speed value.

Nonetheless the results of the measurement uncertainty sensitivity analysis show that these effects do still influence the MAUPAT and time domain analysis results. In addition to global mode shape effects, this explains why some undamaged blades exhibited strong trends (e.g. Figure 58). However, the data processing approach presented in this chapter (i.e. the use of σ as a parameter) was shown to be sufficiently robust to deal with these uncertainties.

4.7 Conclusions

In this chapter it has been shown that ELDV is viable as an on-line blade condition monitoring tool for multi-blade rotors. Employing both NHFA and time domain analysis on ELDV measurements from a test rotor at two different measurement positions, the parameters yielded were successfully used to train ANNs for the purpose of identifying and quantifying blade deterioration.

It is demonstrated both numerically and experimentally that run-up and run-down ELDV signatures are valuable in approximating the first bending natural frequencies of individual blades and can serve as an additional condition monitoring parameter.

With the aid of sensitivity analyses, it was established that measurement uncertainties in the ELDV measurement techniques do affect the results significantly. The major sources of error were identified to be speckle noise signal dynamics as well as laser misalignment. However the signal and data processing approaches presented in this chapter were shown to be sufficiently robust to deal with these effects.

The work of this chapter is contained in the article titled *"Eulerian laser Doppler vibrometry: Online blade damage identification on a multi-blade test rotor"* (Oberholster and Heyns, In press).

<u>Chapter 5</u> Conclusions and further work

5.1 Conclusions

This thesis focussed on developing suitable signal processing techniques for ELDV measurements performed on axial-flow turbomachinery blades for the purpose of on-line condition monitoring and damage detection.

From the literature study, it became apparent that little work has been done in the area of ELDV measurements albeit that this area has been studied since the late 1960s.

In Chapter 2, the characteristics of ELDV were analytically studied on a simple cantilever beam based on the Euler-Bernoulli theory for continuous beams. It was shown that, for the cantilever beam translating at a constant speed relative to a stationary LDV, the observed vibration response consists of the combined effects of the amplitude modulation of the various cantilever beam generalized coordinates by their respective (and now time-dependent) characteristic functions. This observation was verified experimentally for a cantilever beam excited at discrete frequencies and moving at slow speeds relative to the LDV. An interpolation approach was proposed and evaluated for the simulation of the ELDV measurement technique in a FEM. Employing reference matrices called LVRMs, it was shown that ELDV can be approximated for various scanning speeds using a fixed nodal resolution in the FEM. Following this, the damage detection capabilities of ELDV were demonstrated numerically. The interpolation demonstrated for longitudinally translating cantilever beams was extended to rotor-axial ELDV on rotating blades. Equations were also presented for rotor-circumferential ELDV measurements.

Chapter 3 focused on ELDV measurements applied to a singe-blade axial-flow test rotor with the laser aligned in the rotor-axial direction. ELDV and TLDV measurements were performed at a fixed rotor speed and increasing blade damage levels and it became apparent that phase angle could be used as a damage indicator. This was verified numerically and after a thorough investigation, NHFA was found to be suitable for extracting phase angle information from the ELDV measurements. It is shown both numerically and experimentally that MAUPATs around reference frequencies provide robust blade health deterioration indicators.

The work of Chapter 3 is extended to a five-blade test rotor in Chapter 4. ELDV and TLDV measurements are considered for multiple blade damage cases at various rotor speeds. It was shown numerically that the phase and amplitude discontinuities

observed in the TLDV measurements in both Chapter 3 and Chapter 4, are as a result of the first bending natural frequency of the damaged blade being in close proximity to one of the rotor orders. Evaluating RMS values, it was shown that ELDV Campbell diagrams of the blades are of importance in experimentally determining the blades' first bending mode frequencies.

As expected for a multi-blade rotor, it was discovered during post-processing that blade damage identification from amongst healthy blades required careful consideration. Exhibiting non-monotonic behaviour with increasing damage, it was necessary to calculate the standard deviations of the MAUPATs. By evaluating this parameter at the various reference frequencies, it was shown that it is possible to produce well defined trends indicative of blade damage. Similar results were obtained from two time domain parameters namely RMS and correlation coefficient values. It was demonstrated that multiple ELDV measurement positions are advantageous to accurately identifying blade damage. ANNs were successfully trained on these parameters and blade damage could subsequently be accurately identified and quantified.

A sensitivity analysis of different measurement uncertainties in Chapter 4 showed that these affect the MAUPAT and time domain results significantly. The signal and data processing approaches presented in this chapter were however found to be significantly robust to deal with these effects.

5.2 Further work

In order to extend the work presented in this thesis to a technique that is practically feasible for on-line blade condition monitoring in an industrial rotor, further work is needed. A research project towards this purpose is currently under way at the Eskom Research and Innovation Division in South Africa.

On the test rotor, high efficiency reflective tape was used to ensure sufficient LDV signal strength during measurements. This of course will not be feasible in an actual operating environment. Reflectivity properties will furthermore vary between new and old blades due to deposition in the blade surfaces. Due to operating environments that are not conducive to the operating conditions required for prolonged LDV operation, it will also be necessary to employ fibre optics for laser beam transmission. The flow medium itself may furthermore affect signal strength as well. All these factors need to be taken into consideration in further work.

The test work that was conducted in this thesis was performed on straight flat rectangular blades with low angles of attack. Typical turbomachinery blades are geometrically more complex and have aerofoil profiles and angles of attack varying along the blade lengths. Although these properties will not directly affect the measurements themselves, they may however prescribe the orientation of the laser beam so as to stay within a reasonable incidence angle range for rotor-axial ELDV measurements. Thus the laser beam orientation may not strictly be in the rotor-axial direction, but it will still mainly provide flap wise vibration information of the blades.

It was shown that multiple ELDV measurement positions are advantageous for accurate blade damage identification. However LDVs are expensive. One solution is to develop a fibre optic SLDV where the laser beam is directed by mirrors (as with normal SLDVs) to various fibres.

Damage was simulated in a controlled manner on the test rotor by means of slot cuts close to the blade roots. It is necessary to verify the technique on blades with true damage.

A number of parameters were presented that provided robust blade damage indicators. These parameters need to be verified at different blade operating conditions. Further work into identifying additional parameters will be valuable to increase the robustness of the technique.

The proposed condition monitoring technique was successfully demonstrated at up to 1440 RPM. The upper limitations of the technique need to be determined.

The technique presented in this thesis was proven for five blades. The technique needs to be verified on rotors such as turbines with a large number of blades.

An LDV was used to obtain on-line blade vibration measurements in an Eulerian fashion in this research. As mentioned earlier, LDVs are however expensive. It will be valuable to identify other instruments and sensors that will provide on-line Eulerian blade vibration information. The presented signal processing techniques can then be applied to these measurements.